Research Square

Preprints are preliminary reports that have not undergone peer review.
They should not be considered conclusive, used to inform clinical practice,
or referenced by the media as validated information.

Experimental and model-based scalability assessment of pH-shift electrolyzers for neutral salt reduction

Jonas Görtz

jonas.goertz@avt.rwth-aachen.de

RWTH Aachen University

Stine Kuhlemann

RWTH Aachen University

Yusuf Alperen Değirmenci

RWTH Aachen University

Jan Haß

RWTH Aachen University

Andreas Jupke

RWTH Aachen University

Research Article

Keywords: Scale-up, Membrane electrolyzer, Electrochemical pH-shift, Water electrolysis, Euler–Lagrange

Posted Date: November 25th, 2026

DOI: https://doi.org/10.21203/rs.3.rs-11593613/v1

License: This work is licensed under a Creative Commons Attribution 4.0 International License.
Read Full License

Additional Declarations: No competing interests reported.

Experimental and model-based scalability assessment of pH-shift electrolyzers for neutral salt reduction

Jonas Görtz[1], Stine Kuhlemann[1], Yusuf Alperen Değirmenci[1], Jan Haß[1], Andreas Jupke[1,2*]

[1]Fluid Process Engineering (AVT.FVT), RWTH Aachen University, Forckenbeckstrasse 51, Aachen, 52074, North-Rhine Westphalia, Germany.

[2]Institute for Bio- and Geosciences (IBG-2), Forschungszentrum Jülich GmbH, Wilhelm-Johnen-Straße, Jülich, 52428, North-Rhine Westphalia, Germany.

*Corresponding author(s). E-mail(s): andreas.jupke@avt.rwth-aachen.de;
Contributing authors: jonas.goertz@avt.rwth-aachen.de; stine.kuhlemann@avt.rwth-aachen.de; yusuf.degirmenci@rwth-aachen.de; jan.hass@avt.rwth-aachen.de;

Abstract

By using water electrolysis to generate protons and hydroxide ions, electrochemical pH-shift electrolyzers offer a promising alternative to the conventional addition of acids and bases. While avoiding the production neutral salt waste and reducing liquid discharge, they can be used, for example, in the biotechnological production of carboxylic acids and in polymer recycling via alkaline hydrolysis. This work presents and assesses a methodology for scaling up electrolyzers from a medium- to a small-sized unit with active electrode areas of 138 cm^2 and 13.7 cm^2, respectively. Ensuring electrochemical similarity, a scale-up methodology was proposed and applied to a developed electrolyzer design. Using carboxylic acids as model systems, scalability was experimentally and numerically evaluated and demonstrated across four current densities between 0.05 and 0.2 A cm^{-2}, two temperatures (20 and 60 °C), and two electrolyte systems (adipic and succinic acid). At all operating conditions, the two scales showed close agreement in protonation efficiency, energy consumption, pH, acid

concentrations, and cell voltages. Complementary CFD simulations based on an Euler–Lagrangian approach provided further insight into flow patterns, gas-phase distribution, and local pH values in the electrolyzers at both scales. The numerical results show strong similarity across the studied geometries. Thus, the proposed methodology is successfully demonstrated, showing that coupling experiments with Euler–Lagrangian simulation enables a priori, model-based scaling of gas-evolving electrochemical reactors and supports transitions between scales.

Keywords: Scale-up, Membrane electrolyzer, Electrochemical pH-shift, Water electrolysis, Euler–Lagrange,

1 Introduction

Electrochemical pH-shift emerged as a promising pH management technique for biotechnological production processes of carboxylic acids and for polymer recycling via alkaline hydrolysis [1, 2]. Conventionally, biotechnological processes for carboxylic acid production rely on the addition of bases to control the pH during fermentation. To recover the thereby produced carboxylate salts, downstream processes use strong acids to shift the pH to acidic conditions, forming the free carboxylic acids [3, 4]. Consequently, the conventional pH management generates equimolar neutral salt waste and liquid discharge, posing ecological and economic challenges [5].

As a substitute for pH agents, electrochemical pH-shift employs water electrolysis to generate hydroxide ions and protons, which can be used in upstream and downstream processes. To perform the pH-shift, the anolyte and catholyte are separated by a cation-exchange membrane (CEM). Thus, pH management simultaneously capitalizes on the hydrogen evolution and oxygen evolution reactions, which increase pH at the cathode and decrease it at the anode [1]. Depending on the concentration and solubility of the target free acid, the anolyte is supersaturated during the pH-shift. As a result, the target carboxylic acids crystallize and can be easily separated from the electrolyte. This concept has been successfully demonstrated in various experimental "proof-of-concept" studies for biotechnologically produced carboxylic acids such as succinic acid [1, 6], itaconic acid [2], and protocatechuic acid [7]. Further, the electrochemical pH-shift has also been demonstrated for the crystallization of terephthalic acid from an alkaline hydrolysate [8].

While these studies demonstrated the technical feasibility of the electrochemical pH-shift, they were mainly conducted in small H-cells with two membrane-separated compartments, were limited to batch operation, and required high potentials due to large electrode distances. To enable continuous operation and process scalability, Kocks et al. [9] proposed an anode chamber design that can be inserted into a standard parallel-plate electrolyzer and evaluated its performance for succinic acid recovery. Their prototype features an active electrode area A_E of 100 cm^2 and is also suitable for gas–liquid–solid flows. This continuous setup represents an important step toward

scaling the process beyond H-cells [10]. However, the proposed design leads to the formation of large dead zones in the inlet area and inner circulation.

To further demonstrate the viability of the electrochemical pH-shift technology, a systematic scalability assessment is essential, as it enables the transition from the mid-laboratory-scale electrolyzer ($A_\mathrm{E} \approx 100\,\mathrm{cm}^2$) to industrial applications ($A_\mathrm{E} \approx 1\,000\,\mathrm{cm}^2$) and small electrolyzers ($A_\mathrm{E} \approx 10\,\mathrm{cm}^2$) for fast screening. For chemical reactors, four similarity criteria, thermal, geometric, electrochemical, and kinematic similarity, can be met [11]. While thermal similarity is easy to achieve, geometric and electrochemical similarity cannot be met simultaneously. Because geometric similarity would result in varying inter-electrode gap δ_E, it is usually sacrificed to keep the current density i and cell potential similar [11]. To ensure electrochemical similarity, Fuller and Harb [12] suggest holding the specific reaction rate

$$r^* = \frac{iA_\mathrm{E}}{\dot{V}_\mathrm{el}}\,, \tag{1}$$

which relates i, and A_E to the electrolyte volumetric flow rate $\dot{V}_\mathrm{el}$, constant. Lastly, kinematic similarity requires that the flow regime and Reynolds number remain similar at all stages of scaling. While a constant channel design can achieve kinematic similarity in the flow frames [13–15], maintaining the gas–liquid flow pattern in open (channel-free) frames is non-trivial. Since δ_E is held constant to implement electrochemical similarity and is an order of magnitude smaller than the width of the electrolyzer, the Reynolds Number is linearly proportional to the superficial electrolyte velocity u^0_el. Hence, kinematic similarity can only be achieved by keeping the superficial electrolyte velocity u^0_el and electro-generated gas volume per flow cross-section A_F constant. However, keeping u^0_el and δ_E constant yields narrow reactors at small scales and wide reactors at large scales because the active electrode height h must stay constant. The requirement of a constant h results from the cross-section A_F being defined as

$$A_\mathrm{F} = w\delta_\mathrm{E}\,, \tag{2}$$

and u^0_el by

$$u^0_\mathrm{el} = \frac{\dot{V}_\mathrm{el}}{A_\mathrm{F}}\,. \tag{3}$$

Inserting equation (1) into (3), $A_\mathrm{E} = w \cdot h$, and rearranging yields

$$h = \underbrace{\frac{r^*\delta_\mathrm{E}}{i}}_{\text{const.}} \cdot \underbrace{u^0_\mathrm{el}}_{\text{const.}}\,, \tag{4}$$

showing that h has to be kept constant to maintain electrochemical ($\frac{r^*\delta_\mathrm{E}}{i}$) and kinematic ($u^0_\mathrm{el}$) similarity. Hence, scaling would solely rely on varying the reactor width w, resulting in impracticable extremely wide designs at industrial scales.

In this study, we present a combined experimental and numerical approach to assess the scalability of pH-shift electrolyzers. We therefore investigate and compare

two different scales ($A_E = 13.7\,cm^2$ and $138\,cm^2$) of an evolution of the anode chamber design proposed by Kocks et al. [9] under various operating conditions. Here, i is varied between $0.05\,A\,cm^{-2}$ and $0.2\,A\,cm^{-2}$. We selected adipic acid (AA) as a model carboxylic acid because it is a key organic dicarboxylic acid used in nylon manufacturing [16] and has not been investigated in prior electrochemical pH-shift studies. To generalize our results, we also conducted experiments at an elevated temperature of 60 °C and in a succinic acid (SA) electrolyte system at both scales.

To gain insights into how scale affects the gas–liquid flow within the electrolyzer, we employed our previously developed four-way coupled Euler–Lagrangian computational fluid dynamics (CFD) model [17] to simulate both scales. Further, we introduced an algorithm to calculate local pH and concentration gradients in the electrolyte based on the simulated flow fields. Finally, we compared the numerical results with experimental findings to assess the developed method for scaling electrochemical pH-shift electrolyzers.

2 Method

Table 1 lists the aqueous electrolyte systems studied. The composition of the catholyte was held constant across all experiments and simulations and consisted of $0.42\,mol\,L^{-1}$ SA ($\leq$ 100,%, Sigma-Aldrich) and $0.5\,mol\,L^{-1}$ Na_2SO_4 (> 99,%, Carl Roth) dissolved in deionized water. Here, we selected AA and SA concentrations close to their solubility limits at 20 °C to enable the crystallization of the target components during the electrochemical pH-shift. The standard anolyte composition for AA experiments consisted of $0.34\,mol\,L^{-1}$ AA ($\leq$ 100 %, Sigma-Aldrich) and $0.34\,mol\,L^{-1}$ sodium hydroxide ($\geq$ 99 %, Carl Roth), resulting in an AA concentration approximately three times higher than its solubility limit at 20 °C. For SA experiments, the anolyte consisted of $0.62\,mol\,L^{-1}$ di-natriumsuccinate ($\geq$ 98 %, Sigma-Aldrich) and $0.5\,mol\,L^{-1}$ Na_2SO_4.

Table 1: Studied catholyte and anolyte compositions for adipic acid (AA) and succinic acid (SA) experiments.

	AA ($mol\,L^{-1}$)	**SA** ($mol\,L^{-1}$)	**Na_2SA** ($mol\,L^{-1}$)	**NaOH** ($mol\,L^{-1}$)	**Na_2SO_4** ($mol\,L^{-1}$)
Catholyte	-	0.42	-	-	0.5
Anolyte AA	0.34	-	-	0.34	0.5
Anolyte SA	-	-	0.62	-	0.5

To accurately depict the dissociation and solubility of the two carboxylic acids, the solubility and dissociation constants of the dicarboxylic acids at a supporting electrolyte concentration of $c_{Na_2SO_4}$=0.5 $mol\,L^{-1}$ are required. To determine the pK_a values of adipic acid, the AA anolyte solution without NaOH was titrated with an alkaline solution containing $0.16\,mol\,L^{-1}$ NaOH and $0.5\,mol\,L^{-1}$ Na_2SO_4. Using the solutions and an EasyMax 102 from Mettler Toledo (Germany), the $pK_{a,1}$ and $pK_{a,2}$ values were determined to be 4.33 and 5.08, respectively. The intrinsic solubility of adipic acid with $c_{Na_2SO_4}$=0.5 $mol\,L^{-1}$ was measured as $0.097\,mol\,L^{-1}$ using the

solid excess method [18]. Kocks [19] reported an intrinsic solubility and $pK_{a,1}$ and $pK_{a,2}$ values for SA at 20 °C with the same supporting electrolyte concentration of 0.578 mol L^{-1}, 3.75, and 5.04, respectively. The resulting dissociation diagrams for both acids are depicted in Fig. S1.

2.1 Experimental setups

Fig. 1 illustrates the experimental setup consisting of the pH-shift electrolyzer, two peristaltic pumps (Masterflex Ismatec, Cole-Parmer GmbH), a power supply (PS 9040-40T, EA Elektro-Automatik), a thermostat (HRC2 control, IKA), two pH meters (HND-R106, KOBOLD Messring), each equipped with a pHenomenal® 221 pH probe (VWR International GmbH), two storage tanks, and a computer for data acquisition. Depending on the scale studied, the peristaltic pumps are equipped with either an Easy-Load pump head (Cole-Parmer GmbH) or an MCP pump head (Cole-Parmer GmbH) for the small- and medium-scale electrolyzers, respectively.

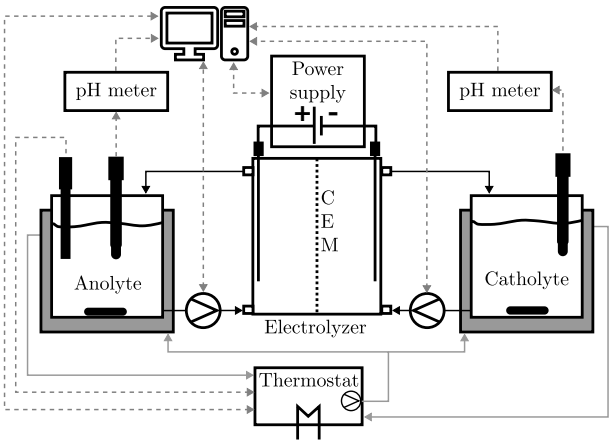

Fig. 1: Schematic illustration of the experimental setup, consisting of the pH-shift electrolyzer, a power supply, two peristaltic pumps, thermostat, two pH-meter, and a computer for data acquisition. The black and gray lines represent the electrolyte and cooling water flow, respectively. The dashed gray lines show the bus lines between the devices.

The used medium-scale electrolyte chamber geometry used is depicted in Fig. 2 (a) and represents an evolution of the prototype proposed by Kocks et al. [9]. Here, we remodeled the inlet area to reduce dead zones and recirculation within the chamber, and A_E amounts to 138 cm^2. Based on A_E, we defined a scaling factor

$$s = \frac{A_E^{scaled}}{A_E^{orig}} \tag{5}$$

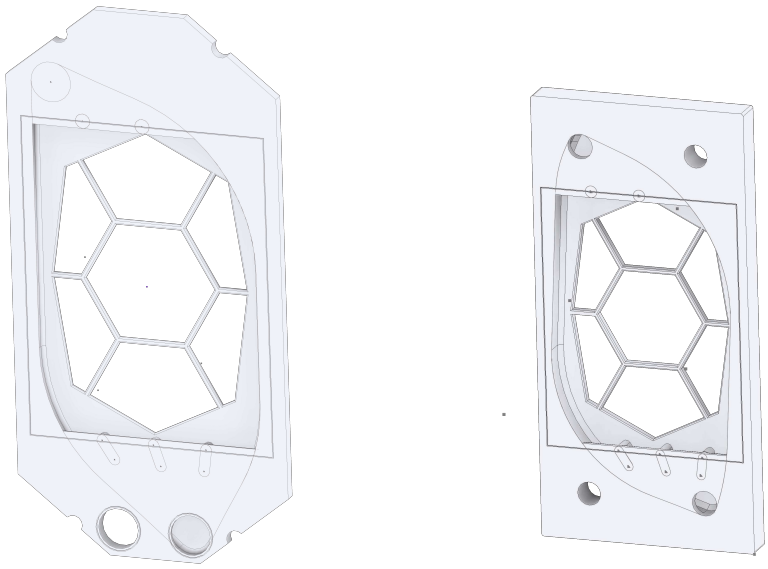

(a) (b)

Fig. 2: Employed prototype with (a) A_{E}=138 cm^2 based on an evolution of the design proposed by Kocks et al. [9]. (b) represents the downscaled (A_{E}=13.7 cm^2) version used in this study. Gray lines indicate the hidden edges of the prototypes.

and using $s \approx 0.1$, we designed a downscaled version, which is depicted in Fig. 2 (b). Hence, the active electrode area of the small-scale electrolyzer amounts to 13.7 cm^2. Regardless of scale, all electrolyzer prototypes were equipped with an Iridium-oxide mixed-metal anode and a nickel cathode and had an electrode-membrane gap of $\delta_{\mathrm{E}} =$ 6 mm. The small- and medium-scale electrolyte chambers were inserted into a Micro Flow Cell® and an Electro MP Cell® from ElectroCell A/S (Denmark), respectively. Fig. S.2 contains an exploded view of the inserted prototype into the Micro Flow Cell®.

Besides δ, i was held constant across both scales to ensure electrochemical similarity. Following eq. (1), this resulted in $\dot{V}_{\mathrm{el}}$ transforming by s, similar to A_{E}. To prevent extremely wide prototypes, the height h and width w were adapted according to $h = w = \sqrt{s}$. Thus, A_{F} and, therefore, u^0_{el} changed by a factor of $\sqrt{s}$. However, the scale-up methodology keeps the electrolyte residence time, τ, constant because h and u^0_{el} are multiplied by the same factor. To simplify the comparison of experiments at both scales, the total volume of anolyte and catholyte was scaled by s as well. Table 2 summarizes the scaling factors used for the different geometrical and operational parameters.

Table 2: Scaling factors for geometrical and operational parameters between the small- and medium-scale pH-shift electrolyzer prototypes based on the active electrode area scaling factor s. In this study, $s = 0.1$.

Parameter	Symbol	Scaling factor
Active electrode area	A_E	s
Current density	i	const.
Electrolyte volumetric flow rate	$\dot{V}_\mathrm{el}$	s
Electrolyzer width	w	$\sqrt{s}$
Electrolyzer height	h	$\sqrt{s}$
Electrode-membrane gap	δ_E	const.
Superficial electrolyte velocity	u^0_el	$\sqrt{s}$
Residence time	τ	const.
Electrolyte volume	V_el	s

2.2 Experimental procedures

Electrolyte solutions were freshly prepared according to the compositions listed in Table 1 before each experiment. Because NaOH pellets were used to adjust the initial anolyte pH for AA experiments, the initial pH varied slightly between 6.5 and 7 across experimental runs. After filling the storage tanks with the respective electrolyte solutions, the peristaltic pumps were started to circulate the electrolytes through the electrolyzer. Simultaneously, the thermostat was turned on to maintain a constant electrolyte temperature. After reaching thermal equilibrium, an initial anolyte sample was taken. Thereafter, the power supply was switched on to galvanostatic operation at the desired current density. For comparability between experiments, anolyte samples were taken at 0.1, 0.3, 0.4, and 0.5 kC of passed charge per A_E. The current, voltage, anolyte and catholyte pH, and temperature were continuously recorded using a computer equipped with a data acquisition software (LabVIEW, National Instruments).

All experiments were run until the anolyte pH reached a value of 3, at which point the second-to-last sample was taken, and the electrolysis was stopped by switching off the power supply. Subsequently, the solution was circulated for an additional 20 min to deplete any remaining supersaturation of AA or SA before taking a final sample. Lastly, the anolyte and catholyte were pumped out of the electrolyzer into the storage tanks, and the electrolyzer was rinsed with deionized water for 20 min. To determine the amount of remaining solids within the tubing and the electrolyzer after each experiment, a sample of the rinsing water was taken. In addition, the final crystal mass is determined by filtering the suspension from the anolyte storage tank, drying the crystals at 50 °C and 200 mbar for 24 hours, and weighing them on a digital precision balance (AX324, Ohaus).

All electrolyte samples were filtered and volumetrically diluted sixfold with the HPLC eluent (2.5 mmol L^{-1} sulfuric acid). Using high-performance liquid chromatography (1100 Series, Agilent Technologies) equipped with a refractive index detector (G1362A, Agilent Technologies) run at 35 °C, the concentration was measured. An organic acid resin column (100 x 8 mm, CS-chromatography-Service) was employed, and a 2.5 mmol L^{-1} sulfuric acid solution was used at a constant flow rate of 0.75 mL min^{-1} and column temperature of 50 °C. The injection volume was set to

10 µL. Calibration curves for AA and SA were recorded prior to the experiments. The retention times of AA, SA, and SO_4^{2-} were determined to be 5.3 min, 4.3 min, and 2.8 min, respectively.

This procedure was followed for all experiments conducted at both scales and for both anolyte systems. Table 3 summarizes the conducted experiments, including the studied scale, anolyte system, current density, volumetric electrolyte flow rate, and electrolyte temperature. The cases marked in bold were replicated twice to assess reproducibility. To assess the protonation efficiency of the pH-shift electrolyzers and

Table 3: Overview of the experimentally and numerically studied current densities, electrolyte systems, and temperature at both scales. Depending on s, the volumetric flow rate amounts to $\dot{V}_{\mathrm{el}} = 0.15\,\mathrm{L\,min^{-1}} \cdot s$. The cases marked with * and ** were replicated twice to assess reproducibility of the small- and medium-scale electrolyzers, respectively.

Anolyte system	**i** ($\mathrm{A\,cm^{-2}}$)	T (°C)
AA	0.05	20
	0.1*	
	0.15	
	0.2**	
AA	0.1	60
SA	0.1	20

eventual membrane losses, we introduced the proton efficiency $\eta_{\mathrm{H^+}}$ by

$$\eta_{\mathrm{H^+}} = \frac{\Delta n_{\mathrm{H^+,acid}} + \Delta n_{\mathrm{H^+,SO_4}} + \Delta n_{\mathrm{H^+,aq}}}{Q \cdot F^{-1}}\,. \tag{6}$$

Here, $\eta_{\mathrm{H^+}}$ relates the consumed protons of the carboxylic acid species ($\Delta n_{\mathrm{H^+,acid}}$), sulfuric acid ($\Delta n_{\mathrm{H^+,SO_4}}$), and pH change of the aqueous solution ($\Delta n_{\mathrm{H^+,aq}}$) to the total amount of produced protons calculated via Faraday's law using charge and the Faraday constant ($Q \cdot F^{-1}$). Therefore, the measured pH value and acid concentrations at the start and end of each experiment are used to calculate changes in speciation for all acid species. To the protons consumed in solution, the amount of crystallized acid is then added. The produced protons are calculated using Faraday's law and the total charge passed during each experiment. The detailed calculation for $\Delta n_{\mathrm{H^+,acid}}$, $\Delta n_{\mathrm{H^+,SO_4}}$, and $\Delta n_{\mathrm{H^+,aq}}$ is provided in the supporting information in equations (S.1), (S.2), and (S.3).

2.3 Numerical multiphase CFD model

To gain insights into the gas-liquid flow field of the anolyte chamber, our previously developed Euler–Lagrangian CFD model [17, 20] was applied to both electrolyzer scales. Here, the Euler–Lagrangian model solved the continuous electrolyte phase using the Reynolds-averaged Navier-Stokes equations (RANS) in combination with a k-ω

SST turbulence model. In contrast to the commonly employed Euler-Euler approach [21, 22], the dispersed, gaseous bubbles were tracked individually as Lagrangian parcels within a cloud. Both phases were four-way coupled, accounting for momentum exchange between both phases and bubble-bubble and bubble-wall collisions [23]. For detailed information regarding the multiphase flow model, the reader is referred to Görtz et al. [17] and [20].

In this work, we introduced additional scalar transport equations to resolve the concentration fields of all involved acid species (H_2AA, HAA^-, HAA^{2-}), H^+, SO_4^{2-}, and HSO_4^-. The transport equations accounted for convection, diffusion, dissociation reactions of the acids, and gas phase fraction by

$$\frac{\partial \left(\alpha_{\mathrm{el}} c_j\right)}{\partial t} - \nabla \cdot \left(D_j \alpha_{\mathrm{el}}^{\mathrm{f}} \nabla c_j\right) + \nabla \cdot \left(\alpha_{\mathrm{el}} c_j\right) = R_j \,, \tag{7}$$

with $j \in \{H^+, A^{2-}, HA^-, H_2A, SO_4^{2-}, HSO_4^-\}$. Na^+, $NaSO_4^-$, and Na_2SO_4 were not considered since they do not directly participate in the dissociation reactions. Here, c_j is the concentration of species j, D_j the corresponding diffusion coefficient, R_j the source term from the dissociation reactions, and $\alpha_{\mathrm{el}}^{\mathrm{f}}$ the interpolated gas phase fraction on the cell faces. The dissociation reactions are solved using the built-in reaction framework of OpenFOAM and can be modeled using forward and backward reactions [24]. The full list of implemented reactions and assumed $\mathrm{p}K_{\mathrm{a}}$ values are tabulated in the supporting information in Table S.1. Diffusion coefficients D_j are listed in Table S.2. The anode reaction was implemented as a boundary condition at the anode surface based on Faraday's law

$$R_{\mathrm{H^+}} = \frac{i}{ZF} \,, \tag{8}$$

where F resembled the Faraday constant and Z number of electrons per produced H^+ ion, respectively. Hence, Z amounted to 1.

2.4 Simulation settings and computational domains

Based on the manufactured prototype geometries depicted in Fig. 2, the electrolyte chambers were approximated using a structured hexahedral mesh created with the *blockMesh* and *snappyHexMesh* utilities from OpenFOAM v12. Based on our previous study [17], we selected mesh distances of 1 mm, 1 mm, and 0.4 mm in the x, y, and z directions, respectively. The sole exception was cells close to the walls of the small prototype, where the x and y spacing was reduced to0.5 mm to represent the geometry better. Fig. 3 shows the computational mesh for both scales of the pH-shift electrolyzer. The total number of cells was to 1.3×10^6 and 3.6×10^6 for the small- and medium-scale electrolyzers, respectively.

Simulations were carried out for all experimentally studied current densities, and volumetric flow rates listed in Table 3 of the AA electrolyte system at 20 °C. Each simulation was run for 25 s and all electrolyte fields were written every 0.25 s. To ensure steady state, we analyzed the number of bubbles in the domain; once steady state was reached, we averaged all electrolyte quantities over the last 5 s, corresponding to the last 20 written time steps. For visualization of the results, the time-averaged fields

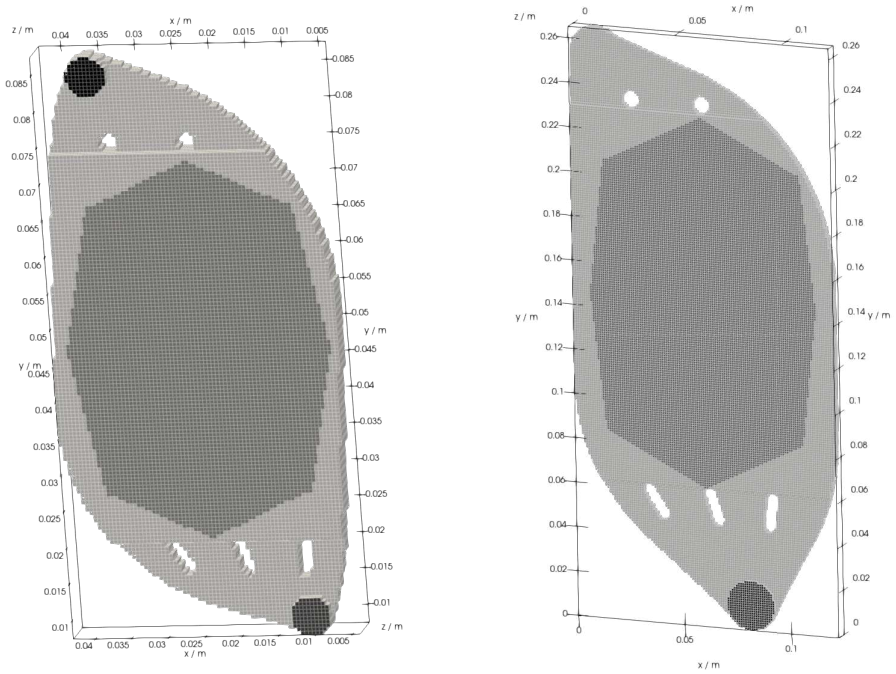

(a) (b)

Fig. 3: Computational mesh of the (a) A_E=13.7 cm^2 and (b) A_E=138 cm^2 pH-shift electrolyzer used for the CFD simulations.

were further averaged in either the x or z direction to obtain 2D plots of the zy or xy planes, respectively.

Boundary conditions for the momentum equations were chosen according to Görtz et al. [17] and Menter et al. [25] and are tabulated in Table S.3. The electrolyte inlet was modeled as a velocity inlet with a turbulent intensity of 5 % and a hydraulic diameter based on the inlet cross-section. The AA concentration is chosen according to Table 1. The initial and inlet pH of 4.36 is chosen such that the acid speciation corresponds to the saturation state S=1.

The small- and medium-scale domains were decomposed into 8 and 16 subdomains, respectively, using the *decomposePar* utility from OpenFOAM v12. Parallel simulations were performed on the CLAIX-2023-HPC cluster at RWTH Aachen University with the corresponding number of cores on Intel Xeon 8468 Sapphire nodes.

3 Results and discussion

Fig. 4 shows the cell potential U, pH, and AA concentration (c_AA) in the anolyte plotted against the transferred electric charge for duplicates of the base case with i=0.1 A cm^{-2}, T=20 °C, $\dot{V}_\mathrm{el}$=0.15 L min^{-1}, and $c_{\mathrm{AA},0}$=0.34 mol L^{-1}. The initial pH of 6.5 rapidly decreases to 6 at the start of the experiments after a charge of 0.15 kC,

corresponding to a duration of 1.8 min. Below a pH of 6, AA starts to buffer, and the electrochemically-produced protons begin to protonate AA molecules, slowing down the decrease in pH. After Q=4 kC, the theoretical AA concentration and pH are 0.34 mol L^{-1} and 4.36, respectively, which equals the solubility limit of AA. Because electrochemical pH-shift crystallization exhibits only marginal metastable zone widths [26], solid AA forms as soon as the solubility limit is exceeded.

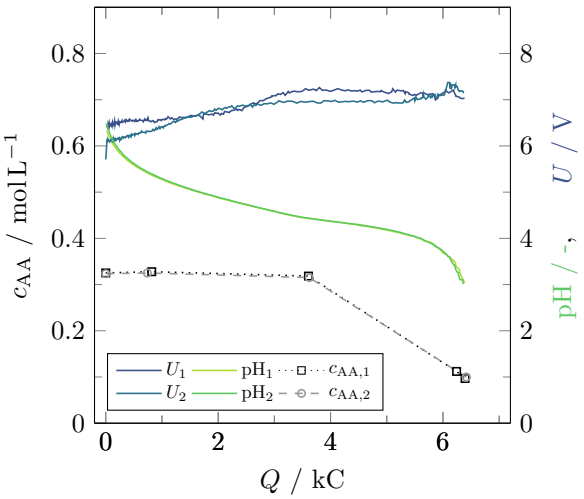

Fig. 4: Experimental results for the duplicate of the base case in the small-scale electrolyzer (A_E=13.7 cm^2) for i=0.1 A cm^{-2}, T=20 °C, $\dot{V}_{el}$=0.15 L min^{-1} and $c_{AA,0}$=0.34 mol L^{-1}.

Once the pH reaches 4, the fully dissociated form of AA is no longer present, thereby drastically reducing the electrolyte's buffering capacity. Furthermore, the crystallization of AA reduces its concentration and, hence, the buffer capacity. As a consequence, the pH value decreases rapidly until it reaches the target value of 3. Here, the initial AA concentration is reduced from 0.34 mol L^{-1} to 0.11 mol L^{-1}.

The cell potential of both experiments starts at 6.2±0.2 V and increases steadily to roughly 7 V at the end of the experiment. The increase in cell potential is mainly caused by the increasing ohmic resistance of the anolyte due to the decreasing concentration of dissociated AA species. In addition, the crystalline AA produced in solution further reduces the anolyte conductivity.

The two experiments in the small-scale prototype demonstrate high reproducibility. The c_{AA} and pH values curves are congruent, and the cell potentials show a similar trend but differ slightly, with a maximum deviation of 0.5 V. Further duplicates are omitted, as the reproducibility is shown to be sufficiently high for the small-scale electrolyzer. The reproducibility of the medium-scale electrolyzer is discussed in the following section, and the results are compared to the small-scale electrolyzer to assess the scalability of the electrochemical pH-shift.

3.1 Experimental scalability assessment across different operating conditions

To assess the scalability of the electrochemical pH-shift, Fig. 5 depicts the experimental results for both cell sizes at i=0.2 A cm^{-2}, T=20 °C, and the AA electrolyte system. To compare the two cell sizes, the pH, cell potential, and AA concentration are plotted against the normalized electric charge q, which is defined as the transferred electric charge Q divided by the electrode area A_E. Here, the cell potential and pH values from the repeated experiment with the medium-scale electrolyzer are illustrated by the filled areas, which indicate the minimum and maximum values. As in the small-scale electrolyzer, the results in Fig. 5 demonstrate excellent reproducibility in the medium-scale electrolyzer.

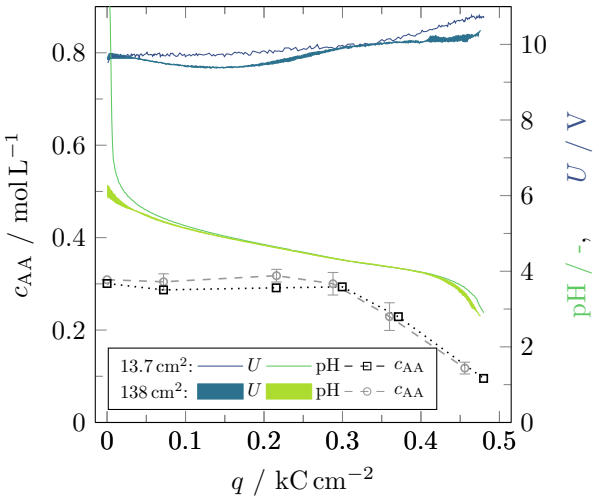

Fig. 5: Experimental results for i=0.2 A cm^{-2}, T=20 °C, and $c_{AA,0}$=0.34 mol L^{-1} and either A_E=138 cm^2 and $\dot{V}_{el}$=1.5 L min^{-1} or A_E=13.7 cm^2 and $\dot{V}_{el}$=0.15 L min^{-1}.

At both scales, the cell potential starts at 9.7 V and increases only slightly to 10.5±0.3 at the end of the experiments. At the small-scale, the cell potential exceeds that of the medium-scale by an average of 0.5 V. This deviation in cell potential could be attributed to the slightly different headspace and outlet designs of the two prototypes, which affect bubble escape and, hence, the ohmic resistance. Further, a greater electrode height increases the average bubble residence time and thus gas phase fraction. However, the trends of the pH and AA concentration of the two sizes fully align, despite a slight offset in initial pH. This agreement between the two sizes showcases the good scalability of the electrochemical pH-shift for AA solutions. Further, the results indicate that mass transfer in the gas-liquid and gas-liquid-solid flows is comparable across the two studied scales.

To further investigate the scalability of the electrochemical pH-shift, Fig. 6 depicts the experimental results for the AA electrolyte system for both electrolyzer sizes at

i=0.05, 0.1, 0.15, and 0.2 A cm^{-2}, 20 °C, and the corresponding volumetric flow rates. In the two-phase region before the onset of crystallization, the pH curve for both electrolyzer sizes and all studied current densities show only marginal deviations. Thus, the agreement across scales confirms that mass transfer is independent of electrolyzer size and operating conditions during the electrochemical pH-shift. After q=0.3 kC cm^{-2}, c_{AA} exceeds the AA solubility, solids form, and the pH trends start to diverge slightly. Here, deviations in the small-scale electrolyzer become apparent at i=0.05 A cm^{-2} and 0.2 A cm^{-2}. The lowest current density shows a rapid decrease in pH, whereas

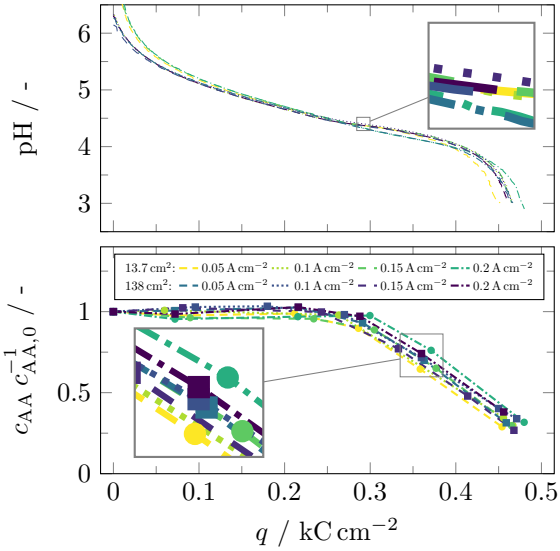

Fig. 6: Measured course of pH (top) and AA concentration (bottom) of all in Tab. 3 tabulated experiments with the AA electrolyte system and T=20 °C at both scales.

the course for the highest current density shows a slightly smaller decrease. This behavior indicates that bubble-induced mixing in the small-scale electrolyzer is more pronounced and that proton cross-over through the membrane becomes significant only at lower pH values. At pH values of 4 and 3, the Na^+/H^+ ratio in the anolyte equals 8000:1 and 700:1, respectively. However, the local pH at the membrane surface is likely to be higher due to concentration gradients, potentially decreasing proton cross-over. Besides the impact of i, the concentration gradients inside the electrolyzer are strongly influenced by the prevailing flow pattern. Numerical [17, 27, 28] and experimental studies [29] suggest that a lower current density results in a segregated flow profile with an intact bubble curtain, with an upward regime near the electrode and a downward or stagnant regime close to the membrane. This flow profile leads to higher concentration gradients and, hence, lower local pH values at the membrane and proton cross-over. Increasing i widens the bubble curtain through bubble-bubble interactions

and enhances the mixing in the z-direction, reducing electrode-membrane concentration gradients [17, 27, 29]. These changes in concentration gradients would increase the local pH at the membrane and explain the observed behavior in the small-scale cell.

In contrast, i does not affect the course of c_{AA} and the pH in the medium-scale electrolyzer. Here, due to the greater number of bubbles in the electrolyzer due to the scaled electrode height ($\sqrt{s}$), mixing mitigates concentration gradients even at the lowest current density studied.

Evaluating the proton efficiency η of both electrolyzer sizes further confirms the previously discussed scalability of the electrochemical pH-shift. Fig. 7 depicts η against the studied current densities for the small- and medium-scale electrolyzers at T=20 °C. Across all experiments, the calculated proton efficiency ranges from 91 % to 99 %. Similar to the discussed pH evolution, lower current densities lead to a slightly higher proton efficiency due to the reduced specific reaction rate r^* (eq. (1)) and less mixing in the z-direction. As i increases, proton efficiency decreases slightly for both scales. However, this effect is only minor compared to the respective deviations of 2.2 % and 4.4 % observed in the repeated experiments for the small- and medium-scale electrolyzers.

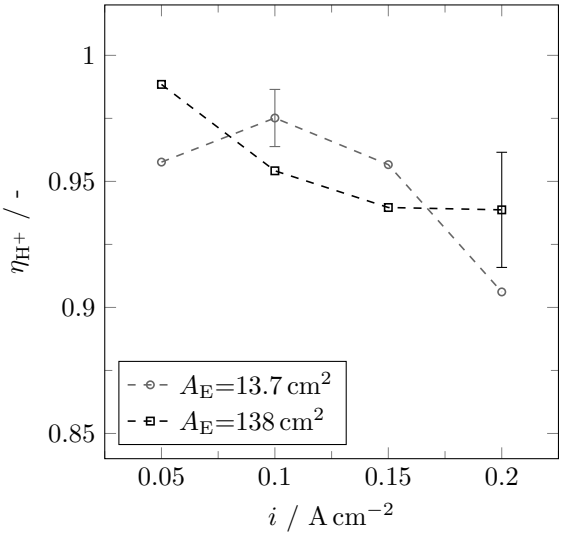

Fig. 7: Proton efficiency as a function of current density for the small- and medium-scale electrolyzers at T=20 °C.

To expand the scalability assessment, further experiments in both electrolyzers were conducted for AA at an elevated temperature of 60 °C and a SA electrolyte system at a temperature of 20 °C for i=0.1 A cm^{-2}. In contrast to the previous results for the AA electrolyte system at 20 °C, the concentration of AA does not exceed the solubility at T=60 °C. As a consequence, no solid formation is observed during the pH-shift electrolysis, and the electrolyzer operates under two-phase gas–liquid flow conditions. Under the two-phase conditions the pH, cell potential, and c_{AA} trajectories

align well between the two studied electrolyzers. Here, the increase in temperature of 40 K reduces the cell potential by roughly 2 V. The average cell voltage, passed specific charge up to the target pH value of 3, and end concentration are tabulated in Table 4.

For the SA electrolyte system, the experimentally obtained cell potential, specific

Table 4: Average cell voltage, passed specific charge up to the target pH value of 3, and end concentration for the pH-shift of AA at T=60 °C and SA at T=20 °C and i=0.1 A cm^{-2}.

	AA, $T = 60\,°C$		SA, $T = 20\,°C$	
Active electrode area / cm^2	13.7	138	13.7	138
Cell potential / V	4.5	4.8	6.2	6.2
Specific total charge / kC cm^{-2}	0.44	0.49	0.66	0.66
End concentration / mol L^{-1}	0.34	0.34	0.79	0.80

total charge, and end concentration for both electrolyzers scales are identical and are added to Table 4. Due to the increased starting concentration $c_{SA,0}$, the experimental duration is increased, and 0.8 kC cm^{-2} is required to reach pH 3. Due to the higher solubility of SA, the onset of crystallization occurs at a pH of 3.2 after q=0.75 kC cm^{-2}, shortly before reaching the final pH value. The detailed curves of pH, U, and c for AA at a temperature of 60 °C and SA at a temperature of 20 °C for i=0.1 A cm^{-2} are presented in Fig. S.3 and Fig. S.4 in the supporting information.

Overall, the results demonstrate the suitability of our proposed method for scaling the electrochemical pH-shift and subsequent crystallization for different current densities, temperatures, and electrolyte systems across small- and medium-sized electrolyzers.

3.2 Model-based study of gas-liquid flow

In addition to the experimental results presented in Section 3.1, numerical simulations of the gas-liquid flow in the electrolyzer were conducted. Fig. 8 depicts the direction of flow and the x-averaged velocity magnitude $\langle|\mathbf{u}_{el}|\rangle_x$ normalized by the scaling factor of the cross-section in the xz-direction ($\sqrt{s^{-1}}$) for the (a-d) small- and (e-h) medium-scale electrolyzers. The y-axis also shows the normalized height of the active electrode, ζ_{h_E}, to facilitate a simple comparison. The number of bubbles within the computational domain for each simulation is depicted in Fig. S.5. It shows that steady state is reached in all simulations after approximately 10 s of simulation time. At both scales, the flow fields at the lowest current density of i=0.05 A cm^{-2} differ from those at higher current densities. Especially for A_E=13.7 cm^2, a segregated two-regime flow is present. Close to the electrode, a strong buoyancy-induced upward flow is present, while the electrolyte near the membrane is stagnant [27]. In the medium-scale electrolyzer, the segregation of the flow is not as pronounced and appears only in the lower half of the displayed section. Increasing i results in a more homogeneous, plug-flow-like velocity profile at both scales. Due to the greater active electrode height in the

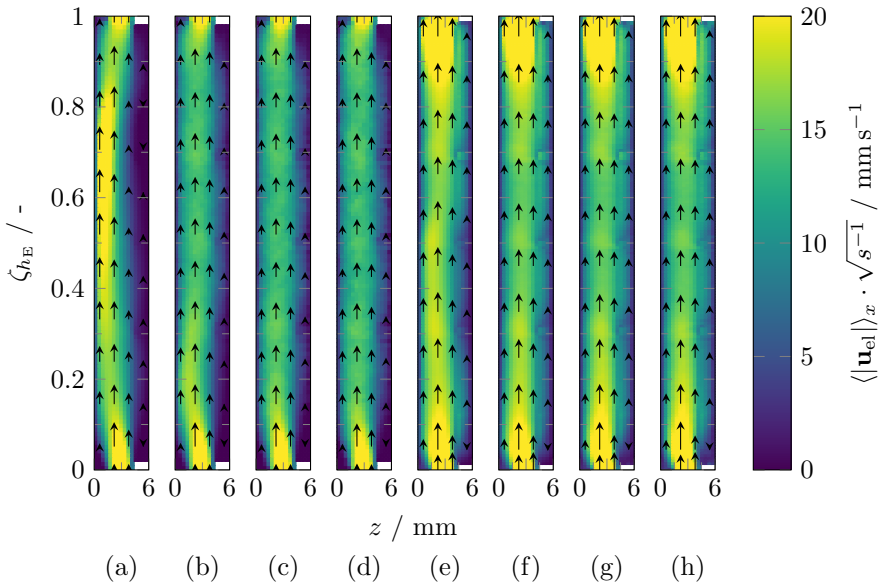

Fig. 8: Simulated time and x-averaged gas-liquid flow field and velocity magnitude in the (a-d) 13.7 cm^2 and (e-h) 138 cm^2 electrolyzer at (a,e) i=0.05 A cm^{-2}, (b,f) i=0.1 A cm^{-2}, (c,g) i=0.15 A cm^{-2}, and (d,h) i=0.2 A cm^{-2}. For better comparison, the velocity magnitude is normalized by the square root of the scaling factor according to the change in u_{el}^0.

medium-scale electrolyzer, the residence time of bubbles increases. Hence, the number of bubbles in the medium-sized electrolyzer exceeds that in the small-sized electrolyzer. Therefore, mixing and the magnitude of the electrolyte flow velocity are enhanced. In comparison with the scaled velocity in the yz-plane that is depicted by black arrows in Figure 8 and remains almost constant across the two scales, the velocity magnitude increases with i is particularly pronounced in the medium-sized electrolyzer. Due to the increased number of present bubbles inside the electrolyzer, the bubble-bubble collision frequency is enhanced, resulting in greater velocity magnitudes and increased mixing.

The discrepancies in flow profiles and patterns across different operating conditions also affect the distribution of bubbles within the reactor. Fig. 9 shows the time- and x-averaged gas phase fraction $\langle\alpha_g\rangle_x$ for both electrolyzer sizes at the four different studied current densities. At i=0.05 A cm^{-2}, the majority of gas bubbles remain close to the electrode, and a distinct bubble curtain is visible. Here, the curtain is more pronounced in the small-scale electrolyzer and stays intact up to ζ_{h_E}=0.75. In the medium-scale electrolyzer and i=0.05 A cm^{-2}, the bubble curtain breaks up at ζ_{h_E}=0.5. The gas phase distribution aligns with the previously discussed flow profiles, with areas of high gas-phase fraction corresponding to upward flow regimes. Here, the homogenization at ζ_{h_E}=0.5 in the medium-scale electrolyzer also marks the transition from a segregated to a homogeneous flow profile.

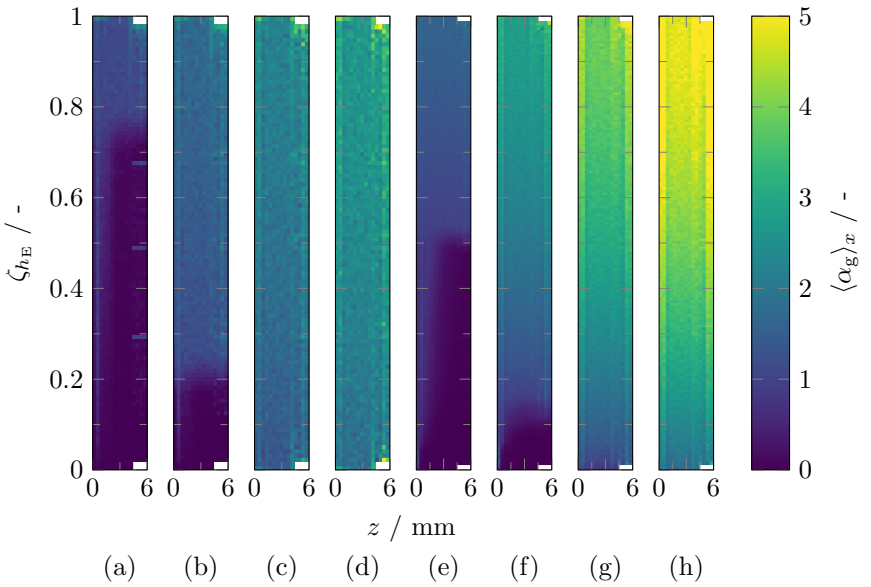

Fig. 9: Simulated time and x-averaged gas phase fraction in the (a-d) 13.7 cm^2 and (e-h) 138 cm^2 electrolyzer at (a,e) i=0.05 A cm^{-2}, (b,f) i=0.1 A cm^{-2}, (c,g) i=0.15 A cm^{-2}, and (d,h) i=0.2 A cm^{-2}.

While at i=0.1 A cm^{-2}, small regions of low gas phase fraction still exist close to the membrane at ζ_{h_E}=0.2 and ζ_{h_E}=0.1 for the small- and medium-scale electrolyzer, respectively. These regions completely vanish at i=0.15 and 0.2 A cm^{-2}. At the higher current densities, the gas phase fraction is evenly distributed along the z-axis, indicating good cross-sectional mixing. Along the relative active electrode height of the medium-scale electrolyzer, the gas fraction increases linearly from the bottom to the top, with the highest gas-phase fractions observed at the top. At the small-scale, this trend is less pronounced, and gas bubbles are present throughout the z-coordinate at ζ_h, indicating poor gas phase discharge from the reactor. Thos impaired gas discharge aligns with the reduced ratio between bubble and outlet size since the bubble size was assumed constant over h_E based on experimental results [30].

The mean gas phase fraction $\overline{\alpha}_g$, which resembles the average over all computational cells of the electrolyzer, is higher in the medium-scale electrolyzer than in the small-scaled electrolyzer at the same current density due to the larger electrode height. In the small-scale electrolyzer, $\overline{\alpha}_g$ increases almost linearly from 0.4 % at i=0.05 A cm^{-2} to 2.4 % at i=0.2 A cm^{-2}, exceeding the corresponding mean values in the medium-scale electrolyzer by roughly 50 %. Here, the mean gas phase fraction increases from 0.7 % to 3.5 %. However, the absolute standard deviation $\sigma(\alpha_g)$ and 95th-percentile $\alpha_{g,95}$ of the gas phase fraction are comparable between the two scales and only deviate by an average of 0.05 % and 0.38 %, respectively. $\sigma(\alpha_g)$ and $\alpha_{g,95}$ increase from 0.6 % and 1.75 ± 0.05 % at i=0.05 A cm^{-2} to 1.1 % and 3.3 ± 0.1 % at i=0.1 A cm^{-2}, 1.35 % and 4.6 ± 0.3 % at i=0.1 A cm^{-2}, and 1.65 % and 5.7 ± 0.4 % at

i=0.1 A cm^{-2}. These values, along with the gas phase distribution illustrated in Fig. 9, demonstrate the similarity between the two scales. The calculated values of $\overline{\alpha}_{\mathrm{g}}$, $\sigma(\alpha_{\mathrm{g}})$, and $\alpha_{\mathrm{g},95}$ are summarized in Tab. 5.

Table 5: Simulated gas phase fraction mean $\overline{\alpha}_{\mathrm{g}}$, standard deviation $\sigma(\alpha_{\mathrm{g}})$, and 95th-percentile $\alpha_{\mathrm{g},95}$ of all computational cells in the small- and medium-scale electrolyzers at different current densities.

	$A_{\mathrm{E}} = 13.7\,\mathrm{cm}^2$			$A_{\mathrm{E}} = 138\,\mathrm{cm}^2$		
i (A cm^{-2})	$\overline{\alpha}_{\mathrm{g}}$ (%)	$\sigma(\alpha_{\mathrm{g}})$ (%)	$\alpha_{\mathrm{g},95}$ (%)	$\overline{\alpha}_{\mathrm{g}}$ (%)	$\sigma(\alpha_{\mathrm{g}})$ (%)	$\alpha_{\mathrm{g},95}$ (%)
0.05	0.4	±0.6	1.7	0.7	±0.6	1.8
0.1	1.2	±1.1	3.2	1.7	±1.1	3.4
0.15	1.8	±1.3	4.3	2.7	±1.4	4.9
0.2	2.4	±1.6	5.3	3.5	±1.7	6.1

3.3 Numerical analysis of local pH values

Based on the velocity and gas phase fraction fields, the concentration fields of the electrolyte species were simulated for an initial pH of 4.36, with the corresponding species distribution. Fig. 10 shows the time- and x-averaged pH value in the (a-d) small- and (e-h) medium-scale electrolyzers at the four studied current densities. Independent of i, the pH value in the bulk electrolyte of the small-scale electrolyzer remains constant at the initial value of 4.36 for an active relative electrode height of $0 < \zeta_{h_{\mathrm{E}}} < 0.3$. Here, only the pH value in the immediate vicinity of the electrode decreases due to electrolysis. Afterward, as $\zeta_{h_{\mathrm{E}}}$ increases, the region affected by the proton production broadens for i=0.1, 0.15, and 0.2 A cm^{-2}, and becomes more pronounced at higher current densities. In contrast, due to the presence of the segregated two-phase flow at i=0.05 A cm^{-2} shown in Fig. 8, the pH of the bulk electrolyte remains almost unchanged over the entire relative electrode height. This different pH course is a direct result of the different gas phase distribution. Due to the stable bubble curtain at the electrode, the local electrolyte velocity is affected by the buoyancy acceleration of the bubbles, resulting in higher local electrolyte velocities that were also depicted in Figure 8. As a consequence, mass transport of produced protons is enhanced in the vertical (y) direction compared to the horizontal (z) direction.

In the A_{E}=138 cm^2 electrolyzer, the pH profile is similar for all four studied current densities. At the electrode boundary, the averaged pH cell values exhibit the lowest values before approaching the bulk pH. Here, the affected distances increase with $\zeta_{h_{\mathrm{E}}}$ and i. At the greatest current density, the affected distance reaches 2.4 mm at $\zeta_{h_{\mathrm{E}}}$=0.9, indicating that the electrolysis affected half of the channel.

To enable a better comparison between both electrolyzer sizes, Fig. 11 depicts the course of the local pH value within a 3 mm distance to the electrode in the (a) $A_{\mathrm{E}} = 13.7\,\mathrm{cm}^2$ and (b) $A_{\mathrm{E}} = 138\,\mathrm{cm}^2$ electrolyzer at i=0.05, 0.1, 0.15, and 0.2 A cm^{-2} and $\zeta_{h_{\mathrm{E}}}$=0.5. For both electrolyzer sizes, the pH at the electrode surface decreases as current density increases. In the small- and medium-sized electrolyzers the pH value at

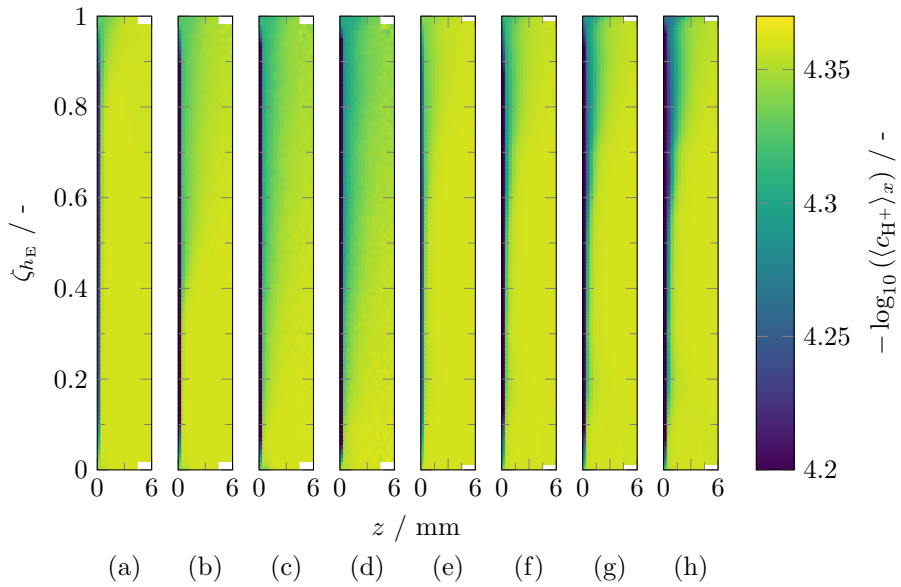

Fig. 10: Simulated time and x-averaged pH value in the (a-d) 13.7 cm^2 and (e-h) 138 cm^2 electrolyzer at (a,e) i=0.05 A cm^{-2}, (b,f) i=0.1 A cm^{-2}, (c,g) i=0.15 A cm^{-2}, and (d,h) i=0.2 A cm^{-2}.

the electrode surface decreases from 4.22 to 4.02 and 4.24 to 3.94 at at i=0.05 A cm^{-2} and i=0.2 A cm^{-2}, respectively. For i=0.1, 0.15, and 0.2 A cm^{-2}, the pH value at the electrode surface is lower in the medium-sized electrolyzer compared to the small electrolyzer. Further, the profiles differ between the two scales. At A_E=138 cm^2, the profiles are flat for $z > 1.6$ mm and exhibit a pH decline towards the electrode, which is proportional to i. While the pH profiles in the small-scale electrolyzer also show a steep decline towards the electrode, the pH in the bulk electrolyte ($z > 1$ mm) is also affected. Here, the pH remains below the inlet value of 4.36, with the difference scaling with i. This difference in the pH profiles indicates reduced mixing inside the small-sized electrolyzer, which can be attributed to the reduced number of bubbles presented in Fig. 9 and the smaller Reynolds number (Re $\propto u^0 \propto \sqrt{s}$). Solely the profile for i=0.05 A cm^{-2} in the small-sized electrolyzer displayed in Fig. 11 differs from the other studied current densities. Due to the presence of the segregated-flow and bubble curtain, the local velocity at the electrode is higher than in other flow patterns [29], resulting in faster mass transport of the produced protons out of the domain. In addition, mass transport in the quasi-steady, segregated flow pattern is lower than in transitional or pseudo-turbulent regimes [27].

The reported pH profiles in Fig. 11 (b) match those reported by Abdi et al. [31], who also report a steep increase followed by a plateau. Further, they also report a similar behavior when studying the impact of different ratios between u^0 and i. The authors report that a reduced ratio between u^0 and i leads to a steeper pH decline

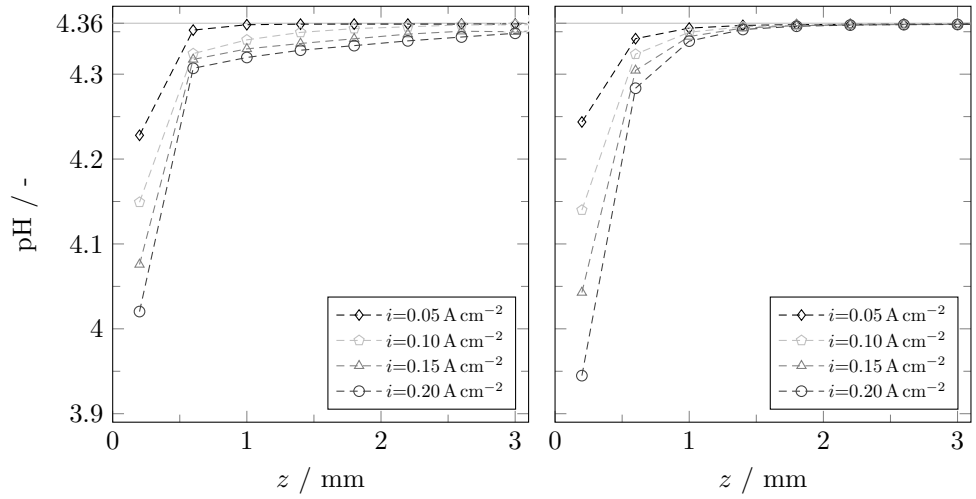

(a) A_{E}=13.7 cm^2 (b) A_{E}=138 cm^2

Fig. 11: Course of local pH value within a 3 mm distance to the electrode (z=0) in the (a) A_{E} = 13.7 cm^2 and (b) A_{E} = 138 cm^2 electrolyzer at i=0.05, 0.1, 0.15, and 0.2 A cm^{-2} and $\zeta_{h_{\mathrm{E}}}$=0.5. The horizontal gray line indicates the inlet pH value of 4.36.

at the á smaller plateau. In our previous study [29], we investigated the impact of different i and u^0 on the present flow profile and showed that segregated, two-regime flows are only present at low u^0 and i. This finding aligns with the results presented in this study, where segregated flow occurs only at i=0.05 A cm^{-2} in the small-scale electrolyzer.

However, except at i=0.05 A cm^{-2} in the small-scale electrolyzer, the pH profiles between the two scales match well and demonstrate the suitability of our proposed method for scaling pH-shift electrolyzers. The numerical results support the experimental scalability assessment and show that the difference at electrode pH is less than 0.08 pH for the studied current densities and electrolyzers. The corresponding supersaturation profiles for the reported pH values are given in the supporting information. They show supersaturations of 1.83 and 1.80 at i=0.05 A cm^{-2}, rising to 2.27 and 2.42 at i=0.2 A cm^{-2}, for the small- and medium-sized electrolyzers, respectively. Despite this higher supersaturation, we observed no corresponding increase in crystallization kinetics in the experimental data at higher current density (see Fig. 6). We attribute this to the inverse scaling of the experimental time with i: reaching a given charge throughput or pH at four times the current density takes roughly a quarter of the time, so the elevated supersaturation acts over a correspondingly shorter period. Hence, the shorter period cancels out the effect of the higher supersaturation.

4 Conclusion

This work presents and assesses a methodology for scaling gas-evolving, electrochemical pH-shift electrolyzers and demonstrates the proposed method for the electrochemical pH-shift crystallization of carboxylic acids. Ensuring electrochemical similarity and a scaling factor of ten, a small (A_E=13.7 cm^2) and medium-scale (A_E=137 cm^2) electrolyzer geometry is developed, and experimentally and numerically assessed. Using carboxylic acids as model systems, we experimentally demonstrate the scalability of electrolyzers for electrochemical pH-shift and subsequent crystallization across four different current densities from 0.05 A cm^{-2} to 0.2 A cm^{-2}, two temperatures, and two electrolyte systems. Across all studied operating conditions, similarity between the two scales in terms of protonation efficiency, cell voltage, pH, acid concentrations, and cell voltages is observed.

Further, CFD simulations of both electrolyzers using an Euler–Lagrangian approach are conducted to gain insights into the gas-liquid flow and mass transfer characteristics. The numerical results demonstrate similarity in terms of flow patterns, gas phase distribution, and pH gradients. Solely at the lowest current density of 0.05 A cm^{-2}, the numerical results exhibit a segregated, two-regime flow pattern [20, 27, 28] in the small-scale electrolyzer, deviating from the other operating conditions. Combined with the corresponding experimental results, our findings indicate that a segregated flow pattern is beneficial, as it limits the mass transport of protons in the electrode-membrane directions and thus prevents proton migration over the membrane. Overall, the strong agreement between experimental and numerical results highlights the capability of the Euler–Lagrange model for the model-based diagnosis of pH-shift electrolyzers [20].

The proposed methodology for scaling electrochemical pH-shift electrolyzers is successfully demonstrated and can be applied to other gas-evolving electrochemical systems. Thereby, the scaling process can benefit from an a priori use of the Euler–Lagrangian model. Future work may focus on increasing the scaling factor to 100 and beyond, as well as investigating different electrolyzer geometries. Here, a change in the direction of inlet and outlet from perpendicular to parallel to the flow direction and an increased diameter of the gas-liquid outlet are of particular interest since they are expected to impact the flow pattern [20] and improve gas removal significantly.

Declaration of competing interest

The authors have no competing interests to declare that are relevant to the content of this article.

Author Contributions Statement

J.G. and J.H. conceptualized the study. J.G. performed the simulations, post-processed and evaluated the results, and wrote the original manuscript draft. S.K. designed and performed all experiments and prepared the visualizations. Y.A.D. developed the numerical model and contributed to the formal analysis. J.H. contributed to the formal analysis and reviewed and edited the manuscript. A.J. acquired funding and supervised the work. All authors reviewed the manuscript.

Acknowledgments

The authors gratefully acknowledge the financial support of "ZeTA" as part of the framework "Modellregion, BioRevierPLUS: InBio, Innovationscluster Integrierte Bioraffinerie, TP2" (no. 031B1135B/031B1135BX), supported by the Federal Ministry of Education and Research (BMBF). Simulations were performed with computing resources granted by RWTH Aachen University under project rwth1989.

References

[1] Kocks, C., Görtz, J., Holtz, A., Gausmann, M., Jupke, A.: Electrochemical Crystallization Concept for Succinic Acid Reduces Waste Salt Production. Chemie Ingenieur Technik **92**(3), 221–228 (2020) https://doi.org/10.1002/cite.201900088 . Accessed 2022-07-07

[2] Gausmann, M., Kocks, C., Pastoors, J., Büchs, J., Wierckx, N., Jupke, A.: Electrochemical pH-T-Swing Separation of Itaconic Acid for Zero Salt Waste Downstream Processing. ACS Sustainable Chemistry & Engineering **9**(28), 9336–9347 (2021) https://doi.org/10.1021/acssuschemeng.1c02194 . Accessed 2022-01-18

[3] Saur, K.M., Kiefel, R., Niehoff, P.-J., Hofstede, J., Ernst, P., Brockkötter, J., Gätgens, J., Viell, J., Noack, S., Wierckx, N., Büchs, J., Jupke, A.: Holistic Approach to Process Design and Scale-Up for Itaconic Acid Production from Crude Substrates. Bioengineering **10**(6), 723 (2023) https://doi.org/10.3390/bioengineering10060723 . Accessed 2025-07-09

[4] Okabe, M., Lies, D., Kanamasa, S., Park, E.Y.: Biotechnological production of itaconic acid and its biosynthesis in Aspergillus terreus. Applied Microbiology and Biotechnology **84**(4), 597–606 (2009) https://doi.org/10.1007/s00253-009-2132-3 . Accessed 2022-12-12

[5] López-Garzón, C.S., Straathof, A.J.J.: Recovery of carboxylic acids produced by fermentation. Biotechnology Advances **32**(5), 873–904 (2014) https://doi.org/10.1016/j.biotechadv.2014.04.002 . Accessed 2026-01-06

[6] Gausmann, M., Kocks, C., Doeker, M., Eggert, A., Maßmann, T., Jupke, A.: Recovery of succinic acid by integrated multi-phase electrochemical pH-shift extraction and crystallization. Separation and Purification Technology **240**, 116489 (2020) https://doi.org/10.1016/j.seppur.2019.116489 . Accessed 2023-03-20

[7] Labib, M., Görtz, J., Brüsseler, C., Kallscheuer, N., Gätgens, J., Jupke, A., Marienhagen, J., Noack, S.: Metabolic and process engineering for microbial production of protocatechuate with *Corynebacterium glutamicum*. Biotechnology and Bioengineering **118**(11), 4414–4427 (2021) https://doi.org/10.1002/bit.27909 . Accessed 2025-02-14

[8] Gausmann, M., Görtz, J., Westarp, W., Jupke, A., Becker, A., Gries, T.: Method for Producing a Monomer from the Polymer Comprising the Monomer. WO2024013254A1, 2023

[9] Kocks, C., Wall, D., Jupke, A.: Evaluation of a Prototype for Electrochemical pH-Shift Crystallization of Succinic Acid. Materials **15**(23), 8412 (2022) https://doi.org/10.3390/ma15238412 . Accessed 2022-11-29

[10] Pletcher, D., Walsh, F.C.: Industrial Electrochemistry. Springer, Dordrecht (1993). https://doi.org/10.1007/978-94-011-2154-5 . http://link.springer.com/10.1007/978-94-011-2154-5 Accessed 2025-11-19

[11] Sulaymon, A.H., Abbar, A.H.: Scale-Up of Electrochemical Reactors. In: Kleperis, J. (ed.) Electrolysis. InTech, ??? (2012). https://doi.org/10.5772/48728 . http://www.intechopen.com/books/electrolysis/scale-up-of-electrochemical-reactors Accessed 2025-11-17

[12] Fuller, T.F., Harb, J.N.: Electrochemical Engineering, First edition edn. Wiley, Hoboken, NJ, USA (2018)

[13] Nelson, V.E., O'Brien, C.P., Edwards, J.P., Liu, S., Gabardo, C.M., Sargent, E.H., Sinton, D.: Scaling CO_2 Electrolyzer Cell Area from Bench to Pilot. ACS Applied Materials & Interfaces **16**(38), 50818–50825 (2024) https://doi.org/10.1021/acsami.4c11103 . Accessed 2026-01-08

[14] Yuan, L., Zhang, L., Feng, J., Jiang, C., Feng, J., Li, C., Zeng, S., Zhang, X.: Upscaling studies for efficiently electric-driven CO2 reduction to CO in ionic liquid-based electrolytes. Chemical Engineering Journal **450**, 138378 (2022) https://doi.org/10.1016/j.cej.2022.138378 . Accessed 2026-01-08

[15] Abarca, J.A., González-Fernández, C., Peralta, C.E., Arruti, A., Santos, E., Díaz-Sainz, G., Irabien, A.: Prototype Validation of a Large-Scale CO_2 -to-Formate Zero-Gap Electrolyzer. ChemSusChem **18**(18), 202501116 (2025) https://doi.org/10.1002/cssc.202501116 . Accessed 2026-01-08

[16] Rios, J., Lebeau, J., Yang, T., Li, S., Lynch, M.D.: A critical review on the progress and challenges to a more sustainable, cost competitive synthesis of adipic acid. Green Chemistry **23**(9), 3172–3190 (2021) https://doi.org/10.1039/D1GC00638J . Accessed 2025-11-19

[17] Görtz, J., Sander, K.M., Jupke, A.: Bubble curtain spread in membrane electrolyzers: Assessing a four-way coupled Euler-Lagrangian model against experimental data **Accepted Manuskript** (2026) https://doi.org/10.1007/s42757-026-0307-0

[18] Beckmann, W. (ed.): Crystallization: Basic Concepts and Industrial Applications. Wiley-VCH, Weinheim, Germany (2013). OCLC: ocn841250907

[19] Kocks, C.U.: Entwicklung und Charakterisierung eines Prototyps für die elektrochemische pH-Shift Kristallisation von biotechnologisch hergestellter Bernsteinsäure. PhD thesis, RWTH Aachen University (2024). https://doi.org/10.18154/RWTH-2024-09388 . Artwork Size: pages 1 Online-Ressource : Illustrationen Pages: pages 1 Online-Ressource : Illustrationen Publication Title: Dissertation Volume: Rheinisch-Westfälische Technische Hochschule Aachen. https://publications.rwth-aachen.de/record/994570 Accessed 2026-01-06

[20] Görtz, J.T.: Experimental and model-based study of gas-liquid-solid flows in pH-shift electrolyzers. PhD thesis, RWTH Aachen University (2025). https://publications.rwth-aachen.de/record/1017302 Accessed 2025-09-22

[21] Colli, A.N., Bisang, J.M.: A two-phase model to predict the enhanced mass transfer by bubble-induced convection in parallel-plate electrochemical reactors. Electrochimica Acta **498**, 144606 (2024) https://doi.org/10.1016/j.electacta.2024.144606 . Accessed 2024-07-15

[22] Liu, C.-L., Sun, Z., Lu, G.-M., Yu, J.-G.: Hydrodynamic characteristics of the two-phase flow field at gas-evolving electrodes: numerical and experimental studies. Royal Society Open Science **5**(5), 171255 (2018) https://doi.org/10.1098/rsos.171255 . Accessed 2025-04-24

[23] Heitkam, S., Sommer, A.-E., Drenckhan, W., Fröhlich, J.: A simple collision model for small bubbles. Journal of Physics: Condensed Matter **29**(12), 124005 (2017) https://doi.org/10.1088/1361-648X/aa56fc . Accessed 2024-06-18

[24] Hlawitschka, M.W., Kováts, P., Zähringer, K., Bart, H.-J.: Simulation and experimental validation of reactive bubble column reactors. Chemical Engineering Science **170**, 306–319 (2017) https://doi.org/10.1016/j.ces.2016.12.053 . Accessed 2025-05-05

[25] Menter, F.R., Kuntz, M., Langtry, R., *et al.*: Ten years of industrial experience with the SST turbulence model. Turbulence, heat and mass transfer **4**(1), 625–632 (2003)

[26] Kocks, C., Krekel, C.M., Gausmann, M., Jupke, A.: Determination of the Metastable Zone Width and Nucleation Parameters of Succinic Acid for Electrochemically Induced Crystallization. Crystals **11**(9), 1090 (2021) https://doi.org/10.3390/cryst11091090 . Accessed 2022-06-28

[27] Alexiadis, A., Dudukovic, M.P., Ramachandran, P., Cornell, A., Wanngård, J., Bokkers, A.: Liquid–gas flow patterns in a narrow electrochemical channel. Chemical Engineering Science **66**(10), 2252–2260 (2011) https://doi.org/10.1016/j.ces.2011.02.046 . Accessed 2022-01-18

[28] Alexiadis, A., Dudukovic, M.P., Ramachandran, P., Cornell, A.: On the stability

of the flow in multi-channel electrochemical systems. Journal of Applied Electrochemistry **42**(9), 679–687 (2012) https://doi.org/10.1007/s10800-012-0426-0 . Accessed 2023-02-07

[29] Görtz, J., Jupke, A.: Exploring the bubble-electrolyte interplay in membrane electrolyzers: PIV measurement of electrolyte flow regimes. International Journal of Multiphase Flow, 105550 (2025) https://doi.org/10.1016/j.ijmultiphaseflow.2025.105550

[30] Görtz, J., Seiler, J., Kolmer, P., Jupke, A.: Raising the curtain: Bubble size measurement inside parallel plate electrolyzers. Chemical Engineering Science **286**, 119550 (2024) https://doi.org/10.1016/j.ces.2023.119550 . Accessed 2024-01-04

[31] Abdi, F.F., Gutierrez Perez, R.R., Haussener, S.: Mitigating voltage losses in photoelectrochemical cell scale-up. Sustainable Energy & Fuels **4**(6), 2734–2740 (2020) https://doi.org/10.1039/D0SE00246A . Accessed 2026-01-08

Supplementary Files

This is a list of supplementary files associated with this preprint. Click to download.

- SupportingInformation.pdf